Electronic Supplementary Information

Fe doping-regulated electron transfer and Co d-band center: boosting ORR/OER catalysis of Co@NCNTs for stable zinc-air batteries

Qihao Wu,[a] Xia Liu,[a] Yuying Feng,[a] Chunyan Wu,[a] Xingwei Zhao,[a] Feng Wen,[a] Guancheng Xu,[a] Li Zhang,*[a, b] Hao Jiang*[b] and Xian Sun*[b]

[a] *State Key Laboratory of Chemistry and Utilization of Carbon Based Energy Resources, College of Chemistry, Xinjiang University, Urumqi 830046, China.*

[b] *School of Chemical Engineering, Xinjiang University, Urumqi 830046, China.*

* Corresponding authors.

E-mail addresses: zhangli420@xju.edu.cn (L. Zhang); jianghao@xju.edu.cn (H. Jiang); xsun@xju.edu.cn (X. Sun)

1. Materials

Unless otherwise stated, all chemical reagents were of analytical grade (AR) and used as received without further purification. Co(II) nitrate hexahydrate ($Co(NO_3)_2 \cdot 6H_2O$, AR, ≥99%), ferrocene ($C_{10}H_{10}Fe$, AR, ≥99%), dicyandiamide ($C_2H_4N_4$, AR, ≥99%), ruthenium dioxide (RuO_2, AR, ≥99.9%), and 20 wt% platinum on carbon (Pt/C, AR) were purchased from Shanghai Aladdin Bio-Chem Technology Co., Ltd. Formic acid (HCOOH, AR, ≥98%) was purchased from Tianjin Zhiyuan Chemical Reagent Plant. Methylamine (CH_3NH_2, 30–33 wt% in methanol, AR) was purchased from Chengdu Kelong Chemical Reagent Factory. Carbon cloth (CC, WOS1011) was purchased from Taobao (China) and ultrasonicated in acetone and 0.5 M H_2SO_4 to remove surface impurities prior to use.

2. Materials characterization

Powder X-ray diffraction (XRD, Bruker D8 advance diffractometer, Cu Kα radiation, λ = 0.15405 nm), Scanning electron microscopy (SEM, Hitachi S-4800), Transmission electron microscopy (TEM, FEI Talos F200X), X-ray photoelectron spectroscopy (XPS, Escalab 250 Xi, Thermo Fisher Scientific), Inductively coupled plasma optical emission spectrometry (ICP-OES, PerkinElmer Optima 8000) and Raman spectroscopy (Raman, Bruker Senterra R 200-L) were used for the structural analysis of as-synthesized samples.

3. Electrochemical measurement

All electrochemical tests were performed at room temperature in a standard three-electrode system using a CHI 760E electrochemical workstation. The Ag/AgCl

or Hg/HgO electrode and graphite rod were used as the reference and counter electrode, respectively. All measured potentials were converted to the reversible hydrogen electrode (RHE) scale according to the Nernst equation ($E_{RHE} = E_{Ag/AgCl\ or\ Hg/HgO} + 0.059pH + E^{\theta}$), where E stands for potential.

3.1. Electrode preparation

Prior to electrochemical tests, a glassy carbon electrode (GCE, 5 mm diameter) was polished with Al_2O_3 slurry (0.05 μm) in a figure-eight pattern, rinsed with deionized water, and ultrasonically cleaned for 10 s. The polished GCE was then tested by cyclic voltammetry (CV) in a solution containing 3 mM $K_3[Fe(CN)_6]$ and 0.1 M KCl. When the peak-to-peak separation (ΔE_p) was less than 80 mV, the electrode was considered well-polished, rinsed with deionized water, and dried at room temperature. For the self-supporting electrode (Fe-Co@NCNTs-5), a circular disk of 5 mm diameter was punched from the as-prepared self-supporting material. This disk was then attached to the pre-treated GCE using 5 wt% Nafion solution as a binder. The mass loading of Fe-Co@NCNTs-5 on CC was approximately 0.5 mg cm^{-2}. For comparison, 2.5 mg of commercial Pt/C (20 wt%) or RuO_2 powder was dispersed in a mixture of 240 μL ethanol and 240 μL deionized water under ultrasonication for 20 min. Then, 20 μL of Nafion solution (5 wt%) was added and the mixture was ultrasonicated for another 1 h to form a homogeneous catalyst ink. An aliquot of 20 μL of the ink was drop-cast onto a circular CC disk (5 mm diameter), yielding a catalyst loading of 0.5 mg cm^{-2}. After drying at room temperature, the CC disk bearing the catalyst was attached to the pre-treated GCE using 5 wt% Nafion

solution as a binder. Thus, both the self-supporting electrode and the reference electrodes were tested under the same configuration (catalyst supported on CC).

3.2. Electrochemical testing for ORR

The electrocatalytic performance of as-synthesized samples evaluation was performed for ORR in a standard three-electrode cell. The electrochemical performance was tested using graphite rods as counter electrodes, adhered as-synthesized sample as working electrode, and Ag/AgCl as reference electrode using electrochemical workstation CHI 760E. Cyclic voltammetry (CV) measurements were performed in N_2 or O_2-saturated 0.1 M KOH solutions with a potential range from 0 to 1.2 V at a scan rate of 50 mV s^{-1}. Linear sweep voltammetry (LSV) curves were recorded during the 1600 rpm rotating disk electrode test. The stability of the catalysts was assessed by chronoamperometry for 1600 rpm at 0.2 V.

The electron transfer number (n) was further obtained from LSV curves measured at various rotating speeds (400–2025 rpm) and calculated according to Eqs. S(1) and (2).

$$\frac{1}{j} = \frac{1}{j_L} + \frac{1}{j_K} = \frac{1}{B\omega^{1/2}} + \frac{1}{j_K} \quad \text{S(1)}$$

$$B = 0.2nFC_o(D_o)^{2/3}v^{-1/6} \quad \text{S(2)}$$

The kinetic current density (j_K) was also calculated from Eq. S(3):

$$j_K = \frac{j_L \times j}{j_L - j} \quad \text{S(3)}$$

where j and j_L are the measured and diffusion-limited current densities (mA cm^{-2}), respectively. ω is the electrode rotating speed (rpm). B is the reciprocal of the slope

determined from the Koutecky–Levitch (K–L) plots and n is the number of electrons transferred per oxygen molecule. F is the Faraday constant (96485 C mol^{-1}); C_o is the concentration of O_2 (1.2×10^{-6} mol cm^{-3}) in solution; v is the kinetic viscosity (0.01 cm^2 s^{-1}), and D_o is the diffusion coefficient of O_2 in 0.1 M KOH (1.9×10^{-5} cm^2 s^{-1}).

The n and H_2O_2 yield for catalysts were examined by rotating ring-disk electrode techniques and calculated according to Eqs. S(4) and S(5).

$$H_2O_2(\%) = 200 \times \frac{I_r/N}{I_d + I_r/N} \quad \text{S(4)}$$

$$n = 4 \times \frac{I_d}{I_d + I_r/N} \quad \text{S(5)}$$

where I_d and I_r are the disk and ring currents, respectively. N (~0.47) is the current collection efficiency of the Pt ring.

3.3. Electrochemical testing for OER

The electrocatalytic performance of as-synthesized samples evaluation was performed for OER in a standard three-electrode cell. The electrochemical performance was tested using graphite rods as a counter electrode, adhered as-synthesized sample as a working electrode, and Hg/HgO as a reference electrode using an electrochemical workstation CHI 760E. LSV curves were obtained in 1 M KOH solution at a scan rate of 5 mV s^{-1} over a voltage range of 1.0 to 1.8 V. The electrochemical AC impedance spectra (EIS) were obtained using an AC current of 5 mV in the frequency range of 100000 to 0.1 Hz, tested at voltages corresponding to a current density of 10 mA cm^{-2}. The double-layer capacitance (C_{dl}) was used to measure the electrocatalytic surface active area of the catalyst. The CV curves of the

as-synthesized samples were tested in 1 M KOH solution at different sweep rates (20, 40, 60, 80, 100 mV s^{-1}) in the potential range of 0.97–1.07 V， and C_{dl} calculated from Eq. S(6).

$$C_{dl} = \frac{j}{v} \quad \text{S(6)}$$

where j is the current density and v is the sweep speed.

3.4. Assembly and testing of ZAB

The ZAB was tested in an electrolyte solution containing 6 M KOH and 0.2 M $Zn(CH_3COO)_2$. Zinc foil was used as the anode, and the air cathode was made from self-supporting electrodes. All tests were carried out in CHI 760E. The specific capacity was calculated and normalized by using the amount of consumed Zn during discharge.

The FZAB consisted of a 1 mm zinc plate as the anode, gel polymer as the electrolyte and Fe-Co@NCNTs-5 as an air cathode. The gel electrolyte was prepared by the following steps: 3 g polyvinyl alcohol (PVA) was dissolved in 30 mL water, magnetically stirred at 90 ℃ for 2 h, and then 3 mL 18 M KOH + 0.02 M $Zn(Ac)_2$ solution was added. After 1 h, a hot light yellow viscous solution was obtained, which was immediately spread on a watch glass to form a 1–2 mm thick gel film and froze for 12 h for use.

4. DFT calculations

In Density Functional Theory (DFT) calculations, structural optimizations were performed under the scheme of generalized gradient approximation (GGA) using the Perdew-Burke-Ernzerhof (PBE) [1] functional, as embedded in the Vienna Ab-initio

Simulation Package (VASP) [2,3]. The projector augmented-wave (PAW) method [4,5] was employed to treat interactions between ion cores and valence electrons. The plane-wave cutoff energy was fixed to 450 eV. The Van der Waals interactions were considered by grime's DFT-D3 method [6,7]. The self-consistent calculations applied a convergence energy threshold of 10-5 eV. The equilibrium geometries and lattice constants were optimized with maximum stress on each atom within 0.02 eV Å-1. During the relaxation, the Brillouin zone with a 3 × 1 × 1 Gamma centered grid was used. Spin polarized calculations were performed for this calculation. The 15 Å vacuum layer was normally added to the surface to eliminate the artificial interactions between periodic images.

For each elementary step, the Gibbs reaction free energy Δ G is defined as the difference between free energies of the initial and final states and is given by the expression:

$$\Delta G = \Delta E + \Delta ZPE - T\Delta S \qquad S(7)$$

where ΔE is the reaction energy of reactant and product molecules adsorbed on catalyst surface, obtained from DFT calculations; and are the change in zero point energies and entropy due to the reaction. Here, the Gibbs energy is corrected by using the VASPKIT code.

Additional model construction parameters

The Co(111) slab model consisted of four atomic layers with a p(3×3) supercell. One Co atom in the topmost layer was substituted by an Fe atom (Fe/Co atomic ratio ≈ 1/9). The experimental Fe/Co atomic ratio from ICP-OES (Co 97.13 wt%, Fe 2.87

wt%) is ≈ 3.1%. The N-doped carbon support was modeled using a 5×5 graphene supercell containing two pyridinic-N, two pyrrolic-N, and two graphitic-N atoms, based on the XPS deconvolution results (Fig. 3f). The Fe-doped Co slab was placed on the N-doped graphene layer with an initial interlayer distance of 3.0 Å, and the geometry was fully relaxed with van der Waals corrections (DFT-D3). All other computational parameters are the same as those described in the main ESI DFT section.

5. Figures

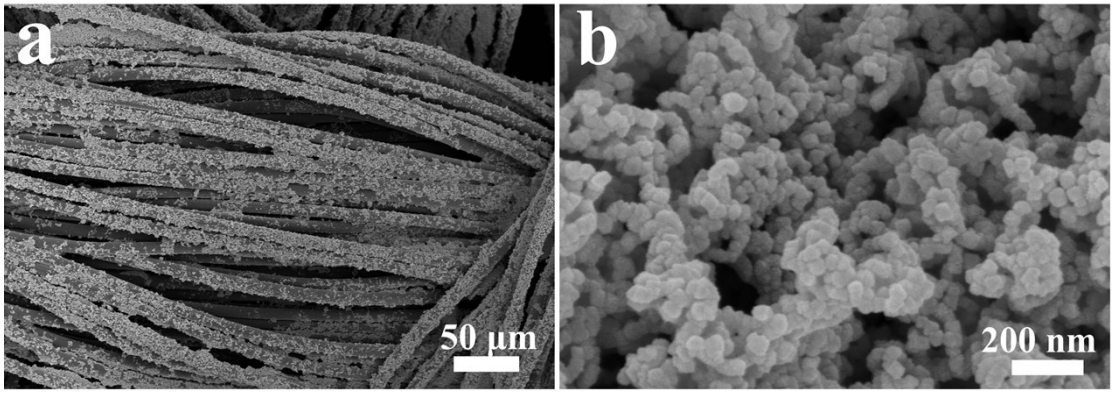

Fig. S1. SEM images of Co_3O_4/CC at different magnifications.

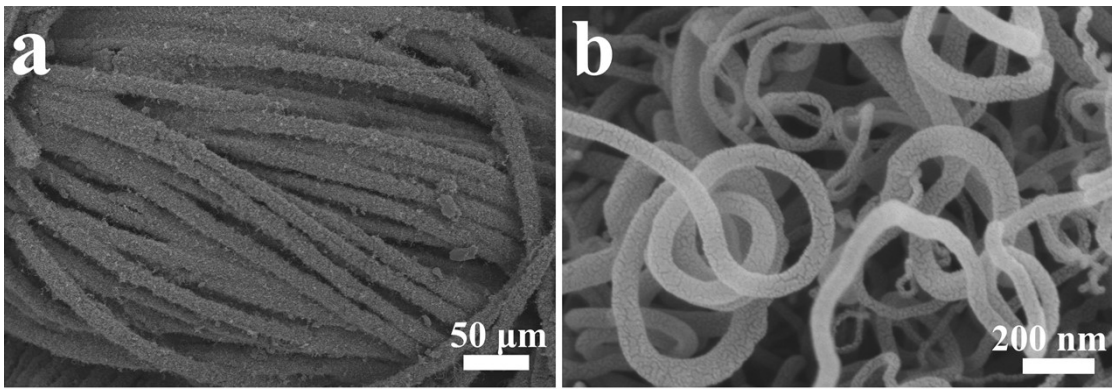

Fig. S2. SEM images of Fe-Co@NCNTs-5 at different magnifications.

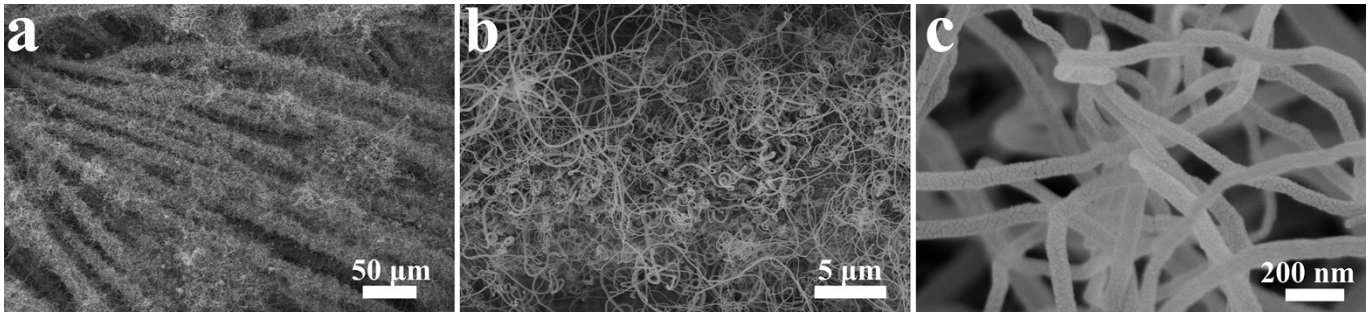

Fig. S3. SEM images of Co@NCNTs at different magnifications.

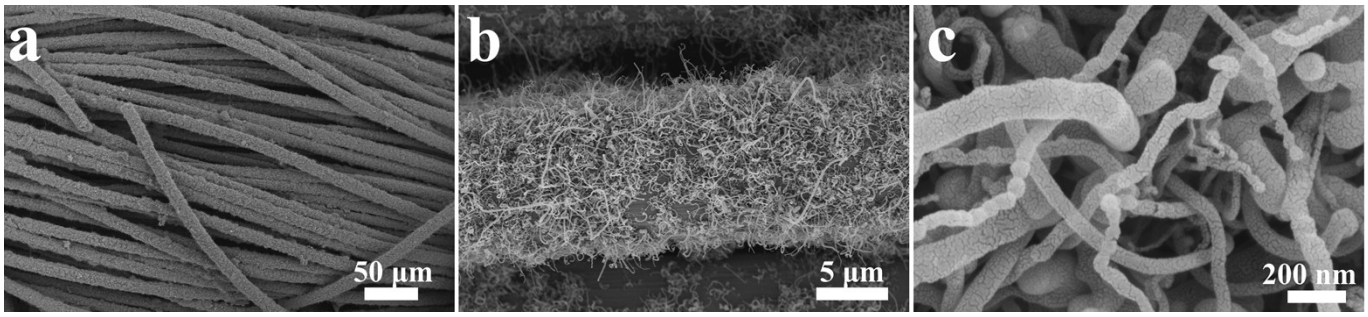

Fig. S4. SEM images of Fe-Co@NCNTs-10 at different magnifications.

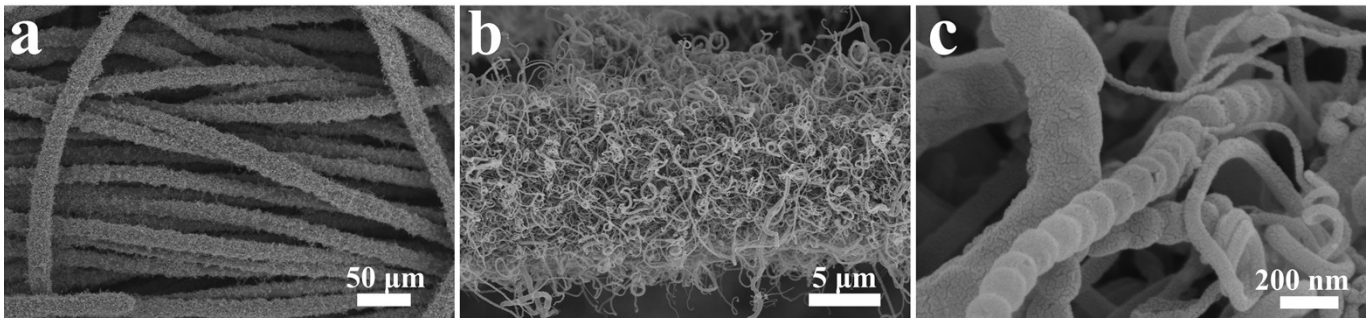

Fig. S5. SEM images of Fe-Co@NCNTs-15 at different magnifications.

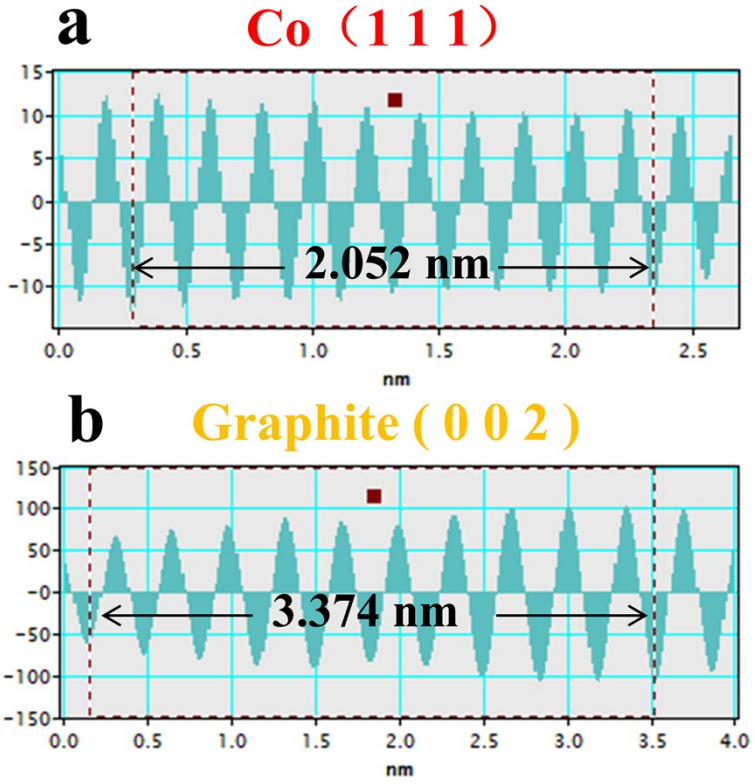

Fig. S6. FFT patterns of (a) Co (111) and (b) graphite (002) lattice fringes.

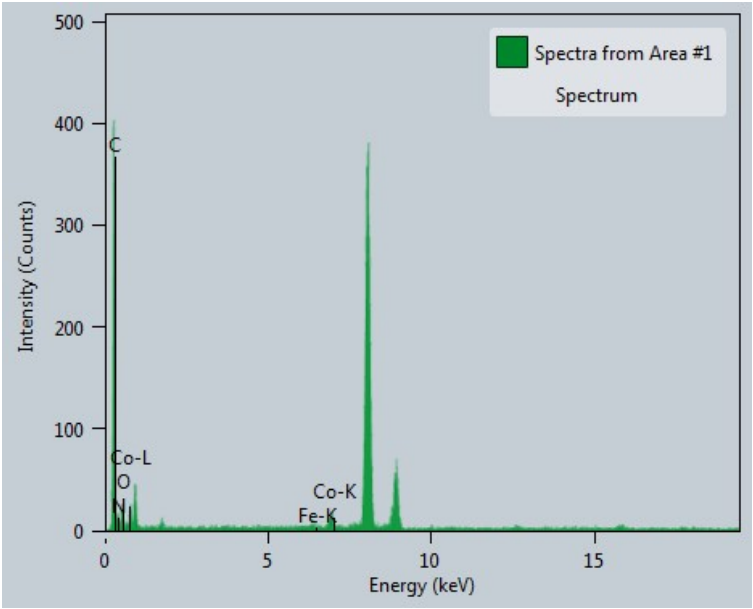

Fig. S7. Raw EDS spectrum of Fe-Co@NCNTs-5 acquired from the region shown in Fig. 2g. Characteristic peaks of C, N, O, Co, and Fe are labeled.

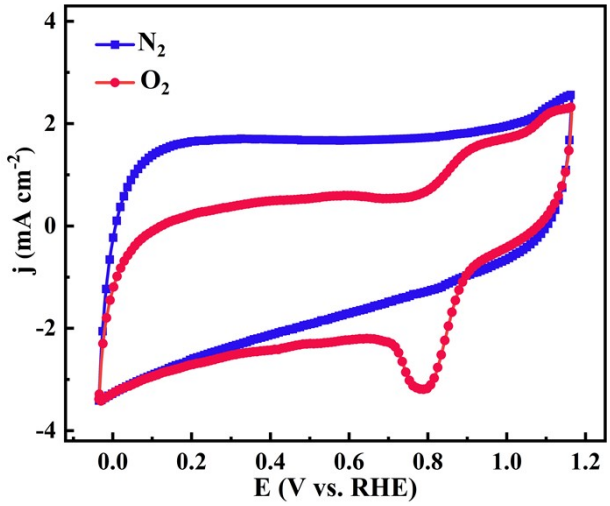

Fig. S8. CV curves of Fe-Co@NCNTs-5 for ORR.

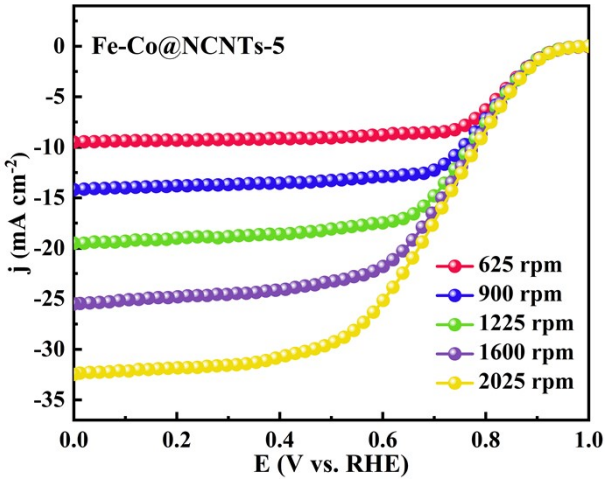

Fig. S9. LSV curves of Fe-Co@NCNTs-5 at different rotation rates.

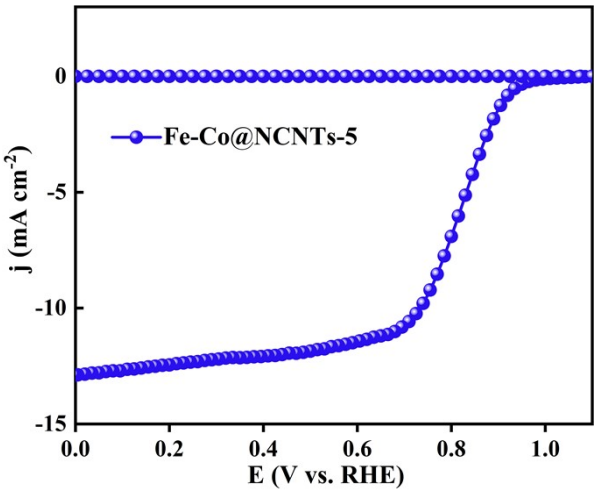

Fig. S10. ORR LSV curves of Fe-Co@NCNTs-5 measured in the rotating ring-disk experiment.

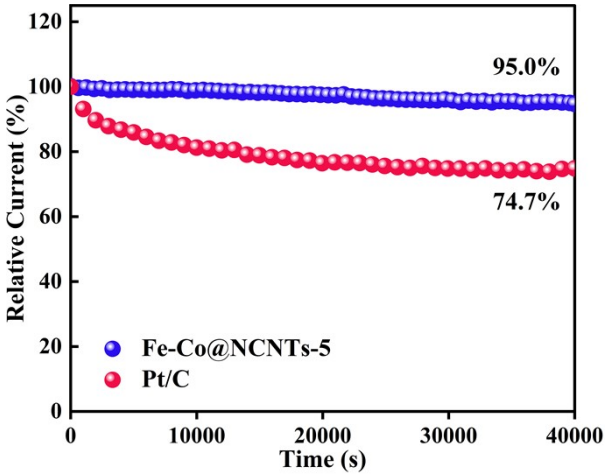

Fig. S11. The relative current–time curves of Fe-Co@NCNTs-5 and 20 wt.% Pt/C

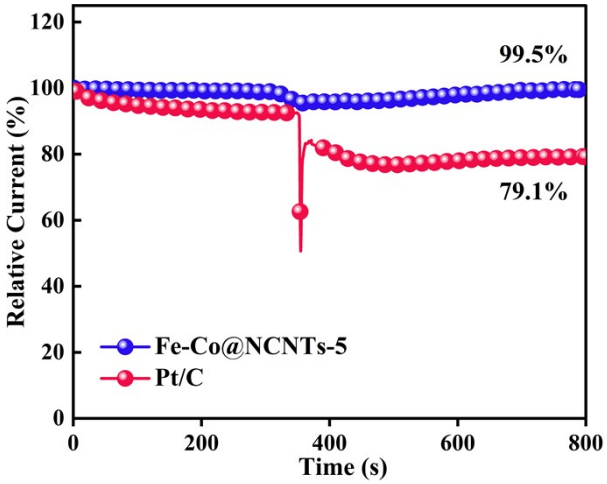

Fig. S12. Methanol tolerance tests for Fe-Co@NCNTs-5 and 20 wt% Pt/C.

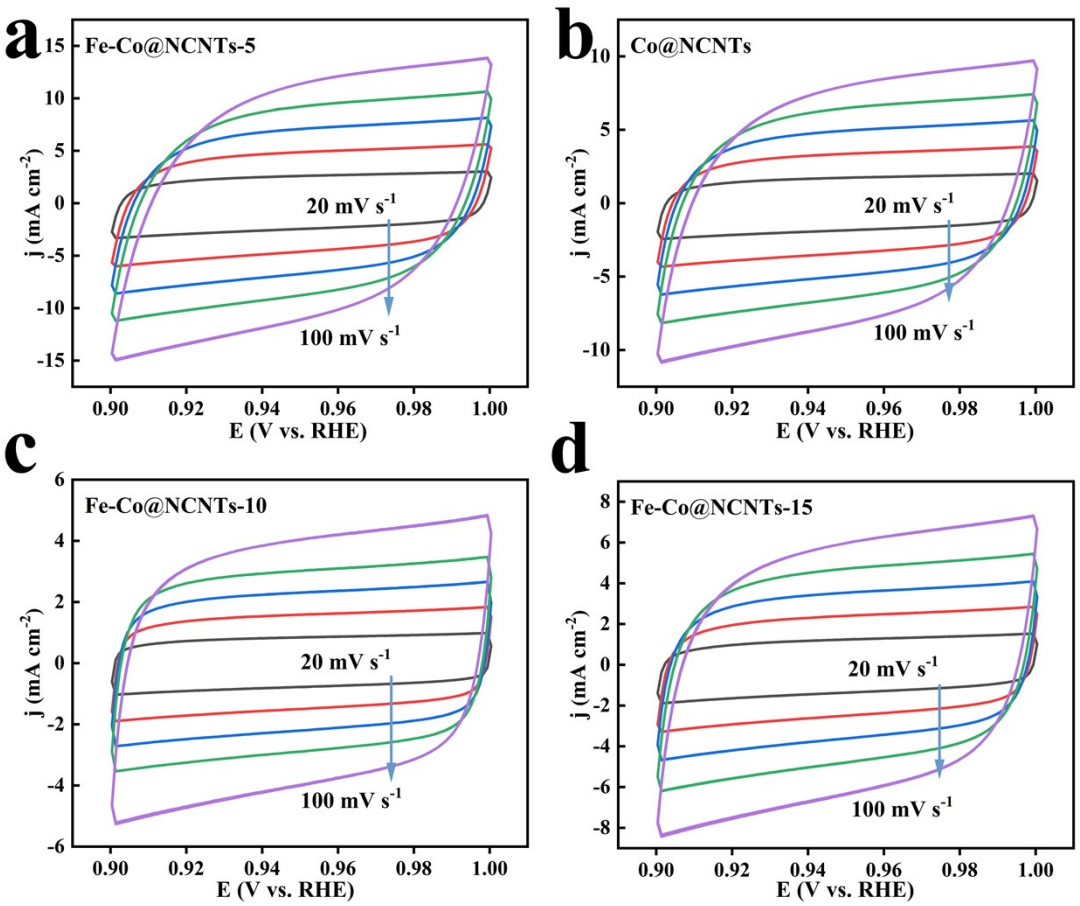

Fig. S13. CV curves of (a) Fe-Co@NCNTs-5, (b) Co@NCNTs, (c) Fe-Co@NCNTs-10 and (d) Fe-Co@NCNTs-15 with increasing scanning rate.

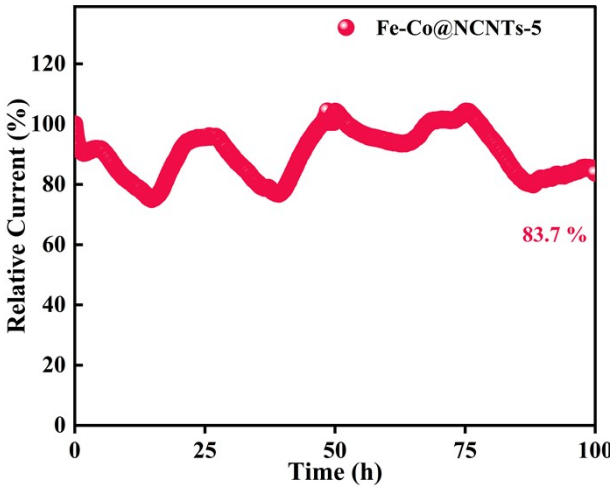

Fig. S14. Current density–time curve of Fe-Co@NCNTs-5.

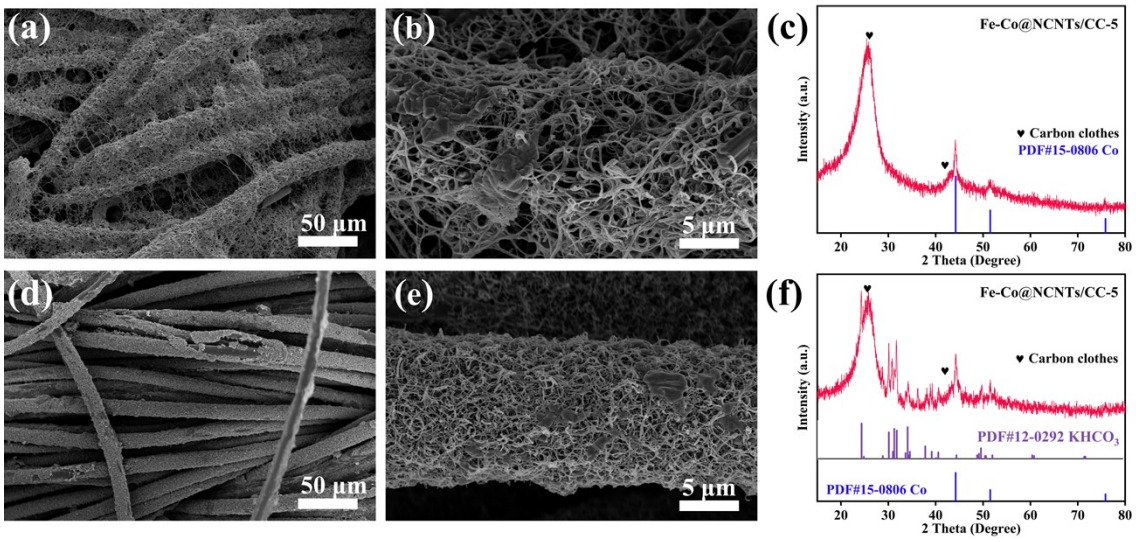

Fig. S15. (a-b) SEM images and (c) XRD pattern after ORR stability test, (d-e) SEM images and (f) XRD pattern after OER stability test.

6. Tables

Table S1. Quantitative EDS results of Fe-Co@NCNTs-5

Element	Mass fraction (wt%)	Atomic fraction (%)
C	86.60	92.73
N	2.85	2.61
O	3.99	3.20
Fe	1.18	0.27
Co	5.39	1.18

Table S2. Comparison of the performance of the Fe-Co@NCNTs-5 with other

reported bifunctional oxygen catalysts in the literature.

Electrocatalysts	$E_{1/2}$ (V vs. RHE)	$E_{j=10}$ (V vs. RHE)	ΔE (V vs. RHE)	Refs.
Fe-Co@NCNTs-5	0.87	1.48	0.61	This work
FeCoN-PDF-T2–2	0.85	1.60	0.75	8
CST-FeCo	0.855	-	-	9
Fe/Co-NGr-3	0.85	1.555	0.705	10
VS-FeCo/Fe-CoS/NSC	0.85	1.57	0.755	11
FeCoNC@Co_2P-NC	0.862	1.536	0.674	12
FeCo@NCNSs	0.863 V	1.629	0.766	13
FeCoNC	0.841	-	-	14
$FexCo_9$−xS_8-NHCS-V	0.8	1.53	0.73	15
f-Fe_1Co_1/CNT	0.88	1.471	0.671	16
Fe/Co LDH	0.84	1.52	0.72	17
Fe_4Co1Ni_2@hNCTs	0.83	1.58	0.75	18
FeCo@NGHS	0.846	1.621	0.755	19
FeCo@NC-900	0.81	1.579	0.769	20
FeCo-N-C	0.8	1.61	0.81	21
FeCo-NCNFs-800	0.817	1.686	0.869	22
Co@MCN1_800	0.81	1.58	0.77	23

References

1. J. P. Perdew, K. Burke, M. Ernzerhof, Generalized Gradient Approximation Made Simple. Phys. Rev. Lett. 1996, 77, 3865–3868.
2. W. Kohn, L. J. Sham, Phys. Rev., 1965, 140, A1133–A1138.
3. P. Raybaud, J. Hafner, G. Kresse, S. Kasztelan, H. Toulhoat, J. Catal., 2000, 189, 129–146.
4. G. Kresse, D. Joubert, From Ultrasoft Pseudopotentials to the Projector Augmented-Wave Method. Phys. Rev. B 1999, 59, 1758–1775.
5. P. E. Blöchl, Projector Augmented-Wave Method. Phys. Rev. B 1994, 50, 17953–17979.
6. S. Grimme, J. Antony, S. Ehrlich, H. Krieg, J. Chem. Phys., 2010, 132, 154104.
7. S. Grimme, S. Ehrlich, L. Goerigk, J. Comput. Chem., 2011, 32, 1456–1465.
8. Y. Kumar, S. Akula, J. Kozlova, A. Kikas, J. Aruväli, M. Käärik, A. Treshchalov, J. Leis, V. Kisand, K. Kukli, E. Kibena-Põldsepp, K. Tammeveski, J. Energy Storage 2024, 86, 111164.
9. Q. Zhu, Y. Wang, L. Cao, L. Fan, F. Gu, S. Wang, S. Xiong, Y. Gu, A. Yu, J. Colloid Interface Sci. 2024, 672, 279–286.
10. M. Mooste, Z. Ahmed, P. Kapitulskis, R. Ivanov, A. Treshchalov, H.-M. Piirsoo, A. Kikas, V. Kisand, K. Kukli, I. Hussainova, K. Tammeveski, Appl. Surf. Sci. 2024, 660, 160024.
11. D. Ko, K. Min, B. Lee, H. Kwon, S.-H. Baeck, J. Power Sources 2025, 625, 235653.
12. T. Yu, X. Cao, R. Song, L. Li, X. Dong, J. Li, X. Wang, X. Zhou, N. Yuan, J. Ding, J. Alloys Compd. 2023, 939, 168678.
13. X. Lin, L. Cui, X. Ding, Y. Chen, Q. Wei, B. Huang, Z. Xie, J. Alloys Compd. 2024, 998, 174805.
14. S. Yang, X. Xue, J. Zhang, X. Liu, C. Dai, Q. Xu, J. Lian, Y. Zhao, G. Li, H. Li, S. Yuan, Chem. Eng. J. 2020, 395, 125064.
15. S.-J. Li, Y. Xie, B.-L. Lai, Y. Liang, K. Xiao, T. Ouyang, N. Li, Z.-Q. Liu, Chin. J. Catal. 2022, 43, 1502–1510.

16. Y.-C. Ting, C.-C. Cheng, S.-H. Lin, T.-Y. Lin, P.-W. Chen, F.-Y. Yen, S.-I. Chang, C.-H. Lee, H.-Y. T. Chen, S.-Y. Lu, Energy Storage Mater. 2024, 67, 103286.
17. N. Allwyn, S. Gokulnath, M. Sathish, ACS Appl. Mater. Interfaces 2024, 16, 20360–20374.
18. W. Tang, J. He, K. Teng, L. Gao, R. Qi, Y. Deng, R. Liu, A. Li, H. Fu, C.-A. Wang, Nanoscale 2022, 14, 17447–17459.
19. Y. Ma, Q. Wang, X. Xiao, Z.-J. Jiang, W. Chen, X. Tian, Z. Jiang, Inorg. Chem. Front. 2025, 12, 608–622.
20. K. Lin, M. Chen, Z. Zhou, H. Huang, J. Zhang, S. Peng, M. Sun, L. Yu, ACS Appl. Energy Mater. 2024, 7, 11172–11183.
21. X.-G. Wu, R. Wang, F. Ma, X.-L. Liu, D.-L. Jia, H.-C. Yang, Y.-P. Liu, Z.-X. Wang, H.-Z. Zheng, Y.-N. Zhang, J. Hou, J.-J. Huang, S.-L. Peng, Rare Metals 2023, 42, 1526–1534.
22. L. Yang, S. Feng, G. Xu, B. Wei, L. Zhang, ACS Sustain. Chem. Eng. 2019, 7, 5462–5475.
23. M. Banerjee, P. Ren, G. Kumar, L. Lindenbeck, B. J. Park, A. Rokicińska, P. Kuśtrowski, A. Slabon, F. Ciucci, R. S. Dey, S. Das, Adv. Funct. Mater. 2025, 36, e19329.